ISBN: 978-3-95450-234-9 ISSN: 2673-5504 doi:10.18429/JACoW-SRF2023-THCAA02

COMMISSIONING OF THE UHH QUADRUPOLE RESONATOR AT DESY

R. Monroy-Villa*[1], A. Gössel, D. Reschke, M. Röhling, M. Schmökel, J.-H. Thie, M. Wiencek
Deutsches Elektronen-Synchrotron, Hamburg, Germany
W. Hillert, C. Martens, M. Wenskat
Universität Hamburg, Institut für Experimentalphysik, Hamburg, Germany
[1]also at Universität Hamburg, Institut für Experimentalphysik, Hamburg, Germany

Abstract

Pushing the limits of the accelerating field or quality factor of SRF cavities beyond pure Nb requires the implementation of specific inner surface treatments, which are yet to be studied and optimized. One of the fundamental challenges in exploring alternative materials is that only samples or cavity cut-outs can be fully characterized from a material science point of view. On the other hand, complete cavities allow for the SRF characterization of the inner surface, while samples can usually only be analysed using DC methods. To overcome this problem, a test resonator for samples, called "Quadrupole Resonator" (QPR), was designed and operated at CERN and a another one later at HZB. In a collaborative project between Universität Hamburg and DESY, a new QPR has been designed, successfully commissioned, and is currently being operated at DESY. It allows for a full RF characterization of samples at frequencies of 0.42 GHz, 0.87 GHz, and 1.3 GHz, within a temperature range of 1.8-20 K and at magnetic fields up to 120 mT. This work presents the design process, which incorporated improvements motivated by mechanical and RF studies and experience. The results from both warm and cold commissioning are discussed as well. More important, the results for the RF tests of a Nb sample after undergoing a series of coarse surface chemistries and an outlook of the further usage of the QPR is presented.

INTRODUCTION

Niobium (Nb) is widely regarded as the optimal material to construct superconducting radio frequency (SRF) cavities for their use in modern particle accelerators. As the accelerating fields within these SRF cavities are approaching their theoretical limit, researchers have explored alternative material and treatments to enhance the cavity performance. Materials such as Nb_3Sn [1, 2], multilayer structures (SIS) [3], and treatments like N-doping [4], N-infusion [5], and mid-T bake [6] of bulk Nb cavities have already demonstrated or have the potential to increase quality factors and maximize achievable fields. However, further investigation is required before cavities manufactures or treated with such recipes can be employed in complete accelerator setups. To expedite alternative material studies, there is a growing interest within the scientific community to characterize small samples of superconducting materials due to the significant cost and time associated with producing and measuring full-scale cavities. Therefore, the development of sample test devices with fast turn-around times are highly valuable for investigating these materials.

RF Characterization Devices

To satisfy this need, laboratories around the world have developed a variety of setups to measure the surface resistance R_s of samples under controlled conditions, such as frequency, temperature, and peak magnetic field. These devices cover operational frequencies from the ultra-high frequency (UHF) range to the W-band, temperatures ranging from 2 K to 20 K and magnetic fields up to 120 mT. Sample diameters are on the centimetre scale and their shapes consist of flat discs, rods, or thin-films. Examples of these setups include TE Host cavities, Sapphire Loaded cavities, SIC, Hemispherical cavities, and Quadrupole Resonators. An overview of these systems can be found in Ref. [7]. These setups also aid in the development and testing of theoretical models of the surface resistance due to the wide space defined by their parameters.

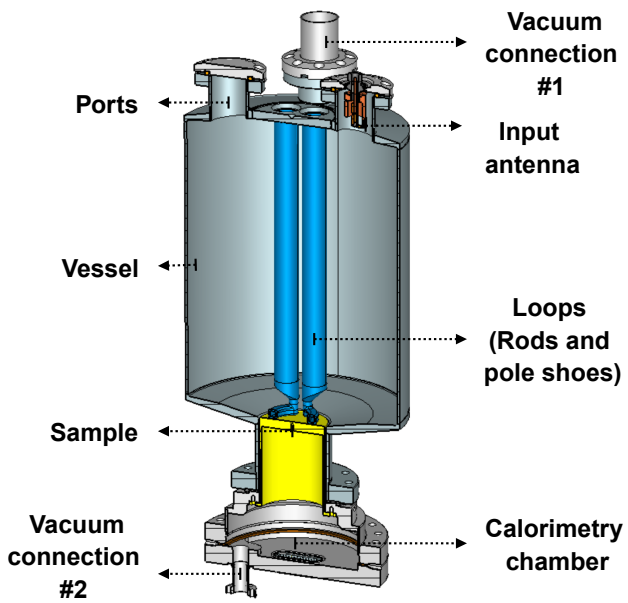

Figure 1: Cross-sectional view of the UHH QPR.

THE QUADRUPOLE RESONATOR

The Quadrupole Resonator was initially developed at CERN (CERN QPR) in 1998 [8, 9]. In the mid-2010s, an optimized version of the QPR (HZB QPR) was reported and brought into operation by Helmholtz-Zentrum Berlin [10,11]. Subsequently, a redesign of the first CERN QPR (called CERN QPR II) was announced in 2017 [12], and was presented in 2019 [13]. Building upon these advancements, a

* ricardo.monroy-villa@desy.de

ISBN: 978-3-95450-234-9 ISSN: 2673-5504 doi:10.18429/JACoW-SRF2023-THCAA02

collaborative effort involving Universität Hamburg, DESY and Universität Rostock [14] has further refined and recently constructed an improved version of the resonator (UHH QPR). A fourth QPR is currently under development at Jefferson Lab [15].

All of the existing QPRs have a similar geometry and utilize similar components. The QPR (depicted in Fig. 1) consists of a high *RRR* niobium screening vessel and four hollow Nb tubes that form a four-wire transmission line, which is welded to the top part of the vessel. These tubes are enclosed pairwise with Nb hollow half rings, known as pole shoes, at the bottom of the rods (highlighted in blue). The rods themselves are hollow to allow for the flow of LHe and to prevent them from warming up during operation. The sample (yellow) consists of a disc welded to a sample cylinder (see Fig. 2) and is mounted to the vessel with a so-called *sample flange*, forming a coaxial gap, as shown in Fig. 3. The top of the QPR has four ports used to install an input

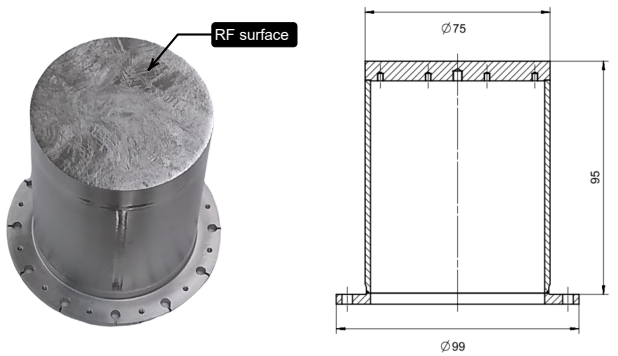

Figure 2: Left) Flat cylindrical QPR sample, with the RF surface ideally being the only part exposed to the electromagnetic field. Right) Cross-sectional view of a QPR sample, with units indicated in millimetres.

and a pick up antenna, and connect to the vacuum system. The enclosed volume within the vessel is typically evacuated to a pressure of 10^{-9} mbar. Below the sample, there is a volume that is not exposed to the RF fields, and is sealed at the bottom of the sample flange with a cable-feedthrough flange. This section forms the calorimetry chamber (see Fig. 3), serving for thermal isolation of the sample from the rest of the resonator and ensuring an adjustable stable sample temperature. This chamber is equipped with four CERNOX^{TM} temperature sensors and a DC heater (50 Ω resistor). Two of those sensors are positioned on the bottom sample surface, while two more are placed at a lower height on the sample tube. The heater is located at the centre of the sample. These auxiliary devices are interconnected within a closed-loop controller that performs a DC power compensation measurement of the sample's surface resistance. At a temperature of 2 K, the QPR has an unloaded quality factor Q_0 of about 10^9. However, since the QPR has a higher sensitivity to microphonics, the external quality factor of the input antenna Q_{ext}^{inp} is set to approximately 10^7 to achieve a coupling $\beta \approx 100$, which increases the bandwidth of the resonance peak. On the other hand, the external quality factor

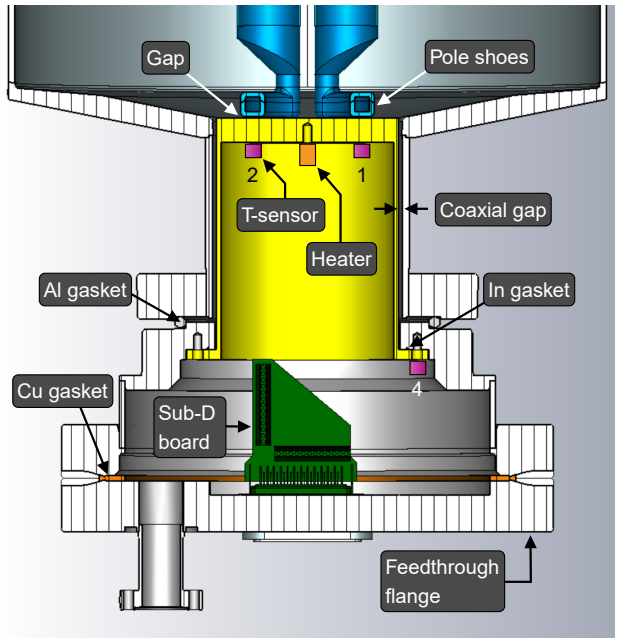

Figure 3: Cross-sectional view of the calorimetry chamber.

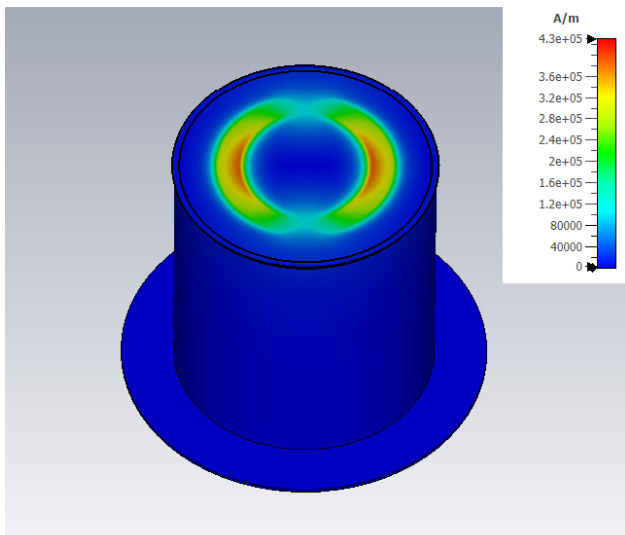

Figure 4: Magnitude of the magnetic field focused on the RF surface of the sample, as simulated in CST Microwave Studio®.

of the pick-up antenna Q_{ext}^{pro} is fixed at nearly 10^{11}, resulting in a coupling of approximately 0.01. These values allow the PLL to maintain the lock of resonance peak of the QPR.

The QPR operates according to the following principle. RF fields are introduced into the test cavity through the input antenna. These fields resonate within the resonator walls, resulting in the generation of quadrupole-like mode distributions of the electromagnetic field. Then, a current is induced in the pole shoes, generating an image current on the sample disc located a fraction of millimetres below them, as can be seen in Fig. 4. The aim is to focus the magnetic field onto the sample surface, maximizing its intensity specifically when exciting the quadrupole mode (operational mode). Furthermore, the RF field of this mode exhibits exponential decays within the coaxial gap up to a frequency of 2.5 GHz. The

ISBN: 978-3-95450-234-9 ISSN: 2673-5504 doi:10.18429/JACoW-SRF2023-THCAA02

energy of the RF field stored in the QPR is measured by a pick up antenna, and this data, combined with the calorimetric technique, enables the determination of the surface resistance of the sample [9, 11].

Calorimetric Measurement Principle

The calorimetric or DC power compensation measurement operates as follows: first, the heater increases the sample temperature from the temperature of the LHe bath T_{bath} to a desired higher temperature T_{int}. The required heating power P_{DC1} is recorded by the controller. Then, the RF power is turned on, and RF dissipation leads to a further increase in the sample's temperature due to Joule heating. The controller decreases the power to compensate for this increase in heat until the temperature of the sample returns to T_{int}. Finally, the new power P_{DC2} is recorded.

Assuming a spatial constant R_{s} across the sample, the process above can be described by

$$\Delta P_{\mathrm{DC}} \approx \frac{1}{2} R_{\mathrm{s}} \cdot \int_{\mathrm{sample}} |H|^2 \, dA. \tag{1}$$

The integral of the H-field can be related to the stored energy U inside the QPR. The measurement of U is carried out based on the principle that the input antenna is overcoupled, and when the RF power is switched off, all energy decays as reflected power through it. By analysing the reflected power P_{ref} at this antenna when the RF power is turned off, U can be calculated according to

$$U \approx \sum_{m}^{N} P_{\mathrm{ref}} \cdot \Delta t, \tag{2}$$

where Δt is the sampling time of the power meter, N is the number of samples and m is the sample at which the RF power is switched off.

Advantages of the QPR

Compared to other sample characterization systems, the QPR offers several advantages. It enables direct measurement of the surface resistance R_{s}, while other devices rely on the relative measurement to a reference sample. The measurements can be performed at typical RF frequencies f, cryogenic temperatures T, and applied magnetic fields B for SRF cavities. For instance, the QPR allows for the study of surface resistance of samples at 1.3 GHz, which is the operational frequency of Nb SRF TESLA-shaped cavities in superconducting LINACs for FELs [16–19]. The QPR facilitates easier sample preparation and exchange with shorter turn-around time and lower cost compared to the same study carried out with multiple cavities operating at different frequencies. The QPR operates at frequencies of 400 MHz and 800 MHz, which corresponds to its first two subharmonics, and enables the study of the residual and BCS resistance contributions [20] or to study frequency-dependent effects [21]. In addition, the QPR allows for measurements of the frequency vs. temperature, London penetration depth λ_L, lower critical magnetic field $H_{c,1}$, and thermal conductivity κ of the sample to determine material parameters such as the critical temperature T_c, the mean-free path ℓ, the superconducting gap Δ or residual resistance R_{res}. Finally, the QPR can accommodate a magnet system to determine the efficiency and sensitivity to trapped flux of a sample and study flux pinning effects [22].

UHH QPR

The UHH QPR was collaboratively designed by Universität Hamburg and DESY, and fabricated at Zanon Research & Innovation Srl (Zanon), following the design of the HZB QPR. The vessel, rods and pole shoes were made of Nb (*RRR*=300). Changes in the design were made due to material availability and operational improvements, such as an increase of the antenna ports radial position by 2 mm and enlargement of their size from 36 mm to 40 mm. The inner diameter of the outer wall of the coaxial tube was reduced by 0.5 mm, which decreased the coaxial gap, as depicted in Fig. 3, from 2 mm to 1.5 mm. The gap between the surface of the pole shoes and the sample RF surface is (0.50 ±0.05)mm. The antennas were fabricated following the HZB design as well (see Fig. 5). The QPR has the following operational frequencies f: Q_1=424 MHz, Q_2=857 MHz, and Q_3=1298 MHz. The samples under investigation have a diameter of 7.5 cm. Additionally, the RF operation is conducted in continuous mode.

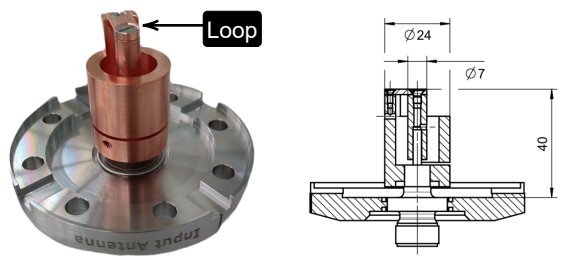

a) Input antenna

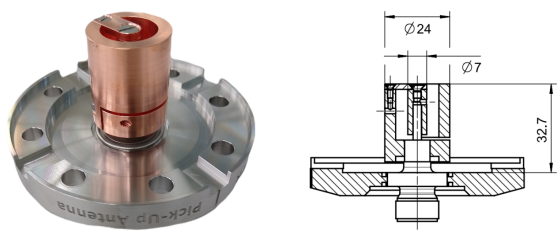

b) Pick up antenna

Figure 5: a) Input and b) pick up antennas are designed to control the coupling by adjusting the angle between the loop area and the field orientation.

At HZB, the rods of HZB's QPR have a mechanical resonance frequency of 100 Hz, which is why the RF pulse repetition rate should not have the same frequency to prevent their excitation or have a 100 Hz signal mixed to the

ISBN: 978-3-95450-234-9 ISSN: 2673-5504 doi:10.18429/JACoW-SRF2023-THCAA02

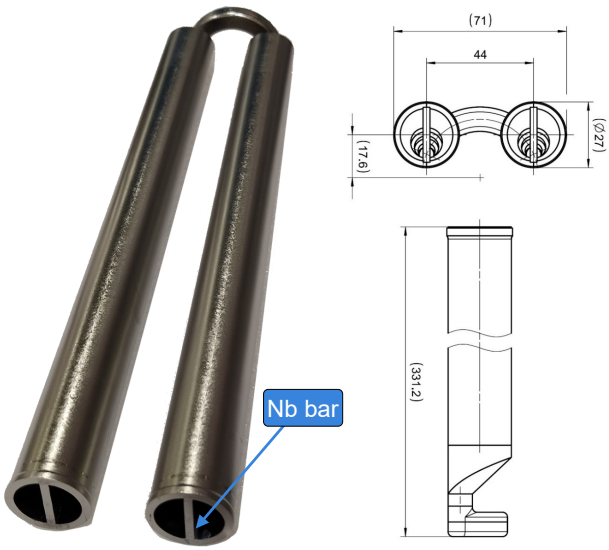

Figure 6: Left) A pair of rods with a pole shoe and an added Nb bar inside each of them to increase their rigidity. Right) Diagram of the rods with pole shoes, dimensions are indicated in millimetres.

carrier frequency [22, 24]. To avoid this issue in the UHH QPR, a rectangular bar made of high purity Nb was welded to the hollow section of the rods to stiffen them and shift the mechanical resonances away from this frequency, as it is the first harmonic of the European power grid operating at 50 Hz. This modification is shown in Fig. 6. A test was conducted to excite the vibrational modes of the rods by hitting the resonator on the top part, where the rods are connected to the vessel. The resulting mechanical spectrum (see Fig. 7) revealed the absence of a mode at 100 Hz. This result show that the QPR exhibits enhanced stability against microphonics in comparison to HZB's design. It has been demonstrated that dipole modes are inevitably excited in all QPR devices due to the presence of the pole shoes, which disrupt the symmetry of the QPR [23]. This results in a greater fraction of dipole mode or even the emergence of a monopole mode

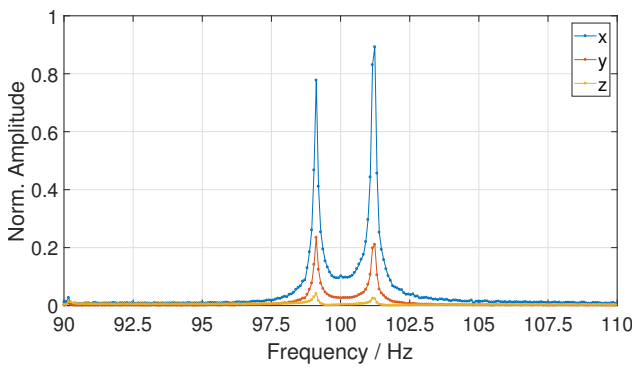

Figure 7: Normalized fast Fourier transform vs. frequency. Three piezoelectric accelerometers sensors mounted on the top part of the QPR measured vibrations in the three dimensions when hitting it in the vicinity of the sensors.

propagating through the coaxial gap, reaching the bottom flange. Consequently, parasitic heating around the bottom area especially at the gasket, causes a temperature rise of the RF surface. This temperature rise is then included in the estimation of the Joule heating, leading to an overestimation of the surface resistance. To address this issue, the sample flange design was optimized by adding cooling channels around the Al gasket area (see Fig. 8), which effectively mitigated the RF surface heating caused by dipole excitation. This modification led to a significant reduction of the adverse effects of dipole modes on the QPR performance.

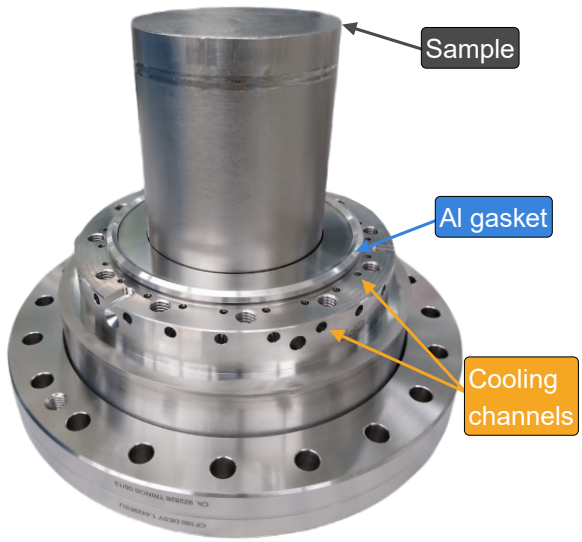

Figure 8: The sample flange with the attached sample and Al gasket incorporates cooling channels to effectively reduce the parasitic heat generated by field propagation within the coaxial gap.

COMMISSIONING OF THE UHH QPR

After fabrication and chemical treatment analogue to SRF cavities at Zanon, the QPR was delivered to DESY. The antennas were installed in an ISO 4 clean room following specific positions and orientations. To achieve an overcoupling strength, the input antenna was placed in port position A, with its loop was oriented at 22°, while the pick up antenna was installed in position B, with its loop oriented at 85°, as shown in Fig. 9. This values were determined from simulations in CST Microwave Studio® (CST). At this position, the external quality factors of the input $Q_{\mathrm{ext}}^{\mathrm{inp}}$ and pick up antennas $Q_{\mathrm{ext}}^{\mathrm{inp}}$ are 10^7 and 10^{11} for the first quadrupole mode (424 MHz), respectively.

The first sample measured with the QPR, on-loan from HZB, underwent a 110 µm BCP as a final treatment step before being delivered to DESY. Since no 800 °C annealing was conducted, it was anticipated that the sample would exhibit a "Q-disease" behaviour [25]. It is worth mentioning that the HZB QPR had not been used to analyse this particular sample before. Therefore, no baseline data was available at the time of its study at DESY. The RF spectrum of the QPR was measured at room temperature using a vector network analyser (Keysight E5061b) after installing antennas and sample.

ISBN: 978-3-95450-234-9 ISSN: 2673-5504 doi:10.18429/JACoW-SRF2023-THCAA02

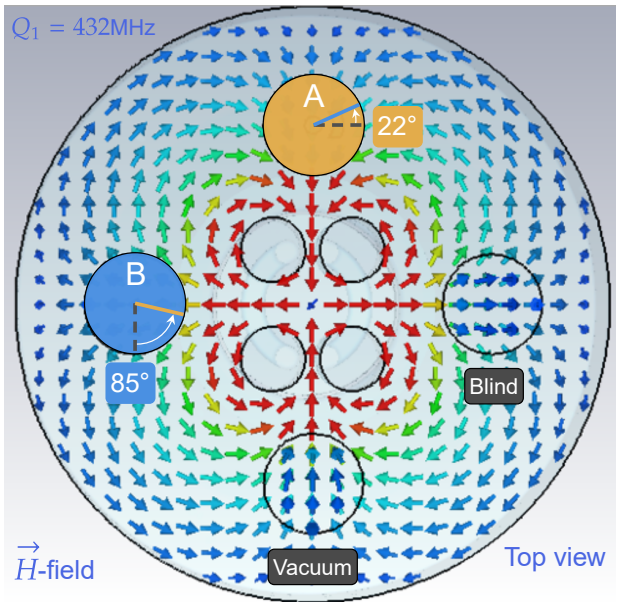

Figure 9: Cutting plane of the QPR perpendicular to the z-axis. The input antenna loop was fixed at 22° in port position A, while the pick up oriented at 85° in position B. The displayed magnetic field distribution represents the quadrupole mode at a frequency of 424 MHz.

The modes are identified with a simulation run in CST using a model that includes metrological information from the QPR throughout fabrication. In addition to the quadrupoles, the QPR also exhibits monopoles and dipoles. Furthermore, eigenmodes of the vessel are observed, referred to as cavity modes. The simulated frequency values exhibited a 7% agreement with the measurements (see Fig. 10). The QPR was then installed in a dedicated insert, which can also support up to three additional 1.3 GHz single-cell cavities. The measurements were conducted using a cryostat that maintained a stable temperature of 1.5 K. The average average pressure inside the cryostat was $\langle p \rangle = 4.72$ mbar with a standard deviation of $\sigma_p = 15.37$ µbar, which corresponded to a temperature variation of $\sigma_T = 0.67$ mK. This ultimately resulted in a frequency change of a few Hz, as reported in Table 1.

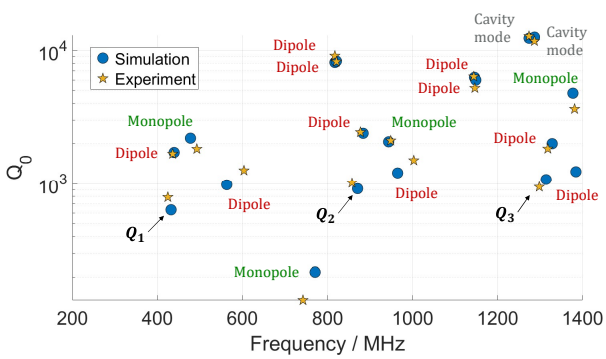

Figure 10: Intrinsic quality factor of the QPR vs. frequency. The spectrum was measured at room temperature, and the modes were identified through simulation in CST.

Table 1: Frequency Uncertainty σ_f Resulting from Cryostat Pressure Variations at 1.5 K

f (1.5 K) / MHz	424	857	1298
σ_f / Hz	24.48	38.99	48.61

FIRST COLD TEST RESULTS

Two measurement campaigns have been conducted to present. In the first campaign, the sample was characterized for the third quadrupole mode, while in the second campaign, it was characterized for all three quadrupole modes. Between the two campaigns, an upgrade was performed to the existing data acquisition system at DESY [26] to be able to measure with the QPR also at frequencies Q_1 and Q_2.

Surface Resistance

Using the calorimetric measurement technique, surface resistance measurements were performed for all quadrupole modes. To determine the stored energy inside the QPR, it was necessary to ensure that the input antenna had the required external quality factor. This was achieved by supplying a forward power P_{for} of 1 W to the QPR. After achieving the steady-state operation, the RF power was turned off, and the traces of the reflected power P_{ref} at this antenna were recorded. These traces were used to calculate the decay time constant τ_{L} and $Q_{\text{ext}}^{\text{inp}}$ for the quadrupole modes. Table 2 shows that the external quality factor of the input antenna is in the order of 10^6 for Q_1, satisfying the overcoupling condition.

Table 2: Decay-time constant τ_{L} and external quality factor of the input antenna $Q_{\text{ext}}^{\text{inp}}$ are determined by analysing the reflected power trace when RF power is switched off.

f / MHz	τ_{L} / ms	$Q_{\text{ext}}^{\text{inp}}$
424	$2.31 \pm 1.10 \cdot 10^{-3}$	$6.16 \cdot 10^6 \pm 2.85 \cdot 10^3$
857	$0.56 \pm 7.10 \cdot 10^{-4}$	$3.04 \cdot 10^6 \pm 3.83 \cdot 10^3$
1298	$0.27 \pm 4.88 \cdot 10^{-4}$	$2.17 \cdot 10^6 \pm 3.98 \cdot 10^3$

The results of the surface resistance vs. temperature of the sample at a constant forward power of 1 W are shown in Fig. 11. These results follow a dependency consistent with the BCS prediction for surface resistance, which is given by Eq. (3).

$$R_{\text{s}}(T) = A \cdot \frac{f^2}{T} \cdot \exp\left[-\frac{\Delta(0)}{k_{\text{B}} T}\right] + R_{\text{res}}, \quad \text{for} \quad T < T_{\text{c}}/2. \quad (3)$$

with $T_{\text{c}} = 9.27$ K. The surface resistance value for Q_1 at 2 K is (22.95 ± 0.76) nΩ, which falls within an acceptable range [23], especially when taking into account the sample's contamination with hydrogen. Although the same forward power was applied, the difference in peak magnetic field B_{peak} on the sample for the different modes is a result of the slightly different field distributions associated with each

ISBN: 978-3-95450-234-9 ISSN: 2673-5504 doi:10.18429/JACoW-SRF2023-THCAA02

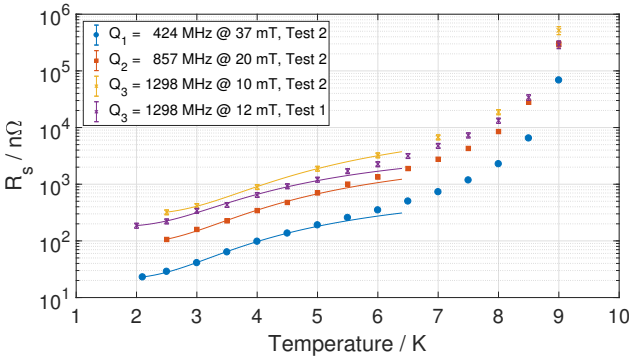

Figure 11: Surface resistance vs. temperature of a Nb QPR sample for all operational frequencies. Continuous lines correspond to the fitting of the data using Eq. (3)

mode. Additionally, it is observed that the same RF power input leads to a different peak magnetic field B_{peak} on the sample. Furthermore, the difference in R_s between the Q_3 curves of Test 1 and 2 is likely attributed to differences in the cooldown rate, although other factors such as multipacting [27] were also investigated during the commissioning.

Surface resistance measurements were conducted to analyse the dependence on $B_{\text{peak, sample}}$ at a constant temperature of 4 K, as shown in Fig. 12. At the peak magnetic field

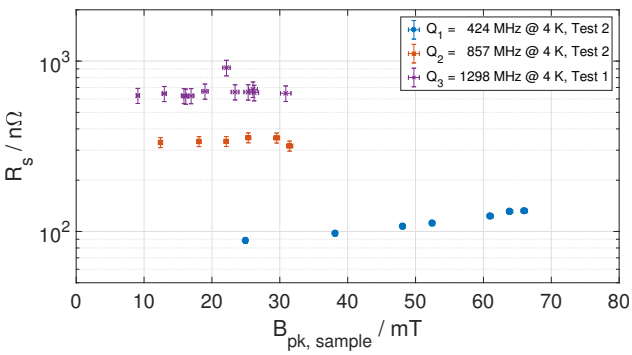

Figure 12: Surface resistance vs. peak magnetic field of a Nb QPR sample for all operational frequencies.

value of approximately 25 mT, the R_s for Q_1 is measured to be (88.32±2.95) nΩ, while for Q_2 it is (355.25±23.82) nΩ. The difference of these two values satisfy the expected increase of f^2, as shown in Eq. (3). The same comparison could not be made for the Q_2 and Q_3 curves since they were measured under different conditions. However, the R_s for Q_3 is (652.75±68.60) nΩ, which is lower than expected based on the same scaling.

Currently, the uncertainty of the R_s measurements is in the worst case of $\sigma_{R_s} = \pm 10\%$, which is calculated with the error propagation of the equipment. However, ongoing investigations are being conducted to explore and address all uncertainties associated with the measurement.

London Penetration Depth vs. Temperature

Measuring the frequency of the QPR as a function of the temperature of the sample leads to the determination of its near-surface material parameters, such as the London penetration depth at 0 K, the mean-free path and the effective penetration depth [21]. The frequency and its change in a given temperature range is related to the change of stored energy, according to Slater [28]:

$$\frac{\Delta f}{f} = \frac{\Delta U}{U}. \tag{4}$$

The change of energy depends ultimately on the penetration of field into the material, which is the London penetration depth λ. The change in frequency is related to the change in penetration depth as follows

$$\Delta\lambda = -\frac{G}{\pi\mu_0 f_0^2}\Delta f, \tag{5}$$

where G is the geometric factor of the sample, which is determined through simulations for each mode, and f_0 is the frequency that remains nearly constant at temperatures below 7 K. It is worth noting that the relationship stated in Eq. (5) remains independent of frequency.

A vector network analyser was employed to determine the spectra of the resonance peak for all quadrupole modes, each subjected to individual thermal cycles using the heater. The spectra were fitted with a Lorentz curve for each temperature, allowing for the determination of the resonance frequency with high accuracy. The resulting frequency change of the sample below the critical temperature T_c for the three quadrupole modes is shown in Fig. 13.

The uncertainty of this measurements is primarily influenced by the cryostat stability, as shown in Table 2. However,

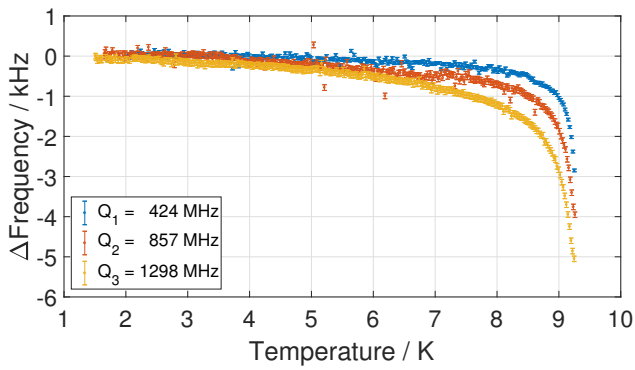

Figure 13: Frequency shift vs. temperature for the three operational QPR frequencies.

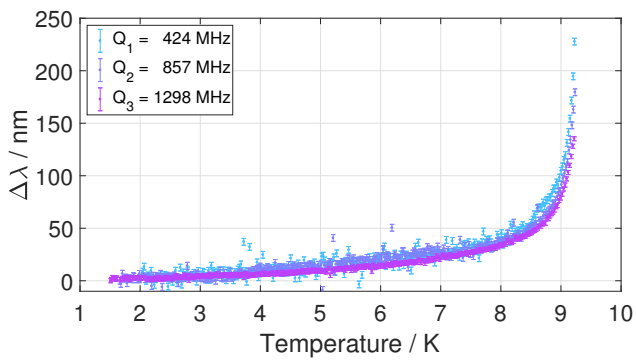

Figure 14: Shift of London Penetration depth $\Delta\lambda$ vs. temperature for the three operational QPR frequencies.

ISBN: 978-3-95450-234-9 ISSN: 2673-5504 doi:10.18429/JACoW-SRF2023-THCAA02

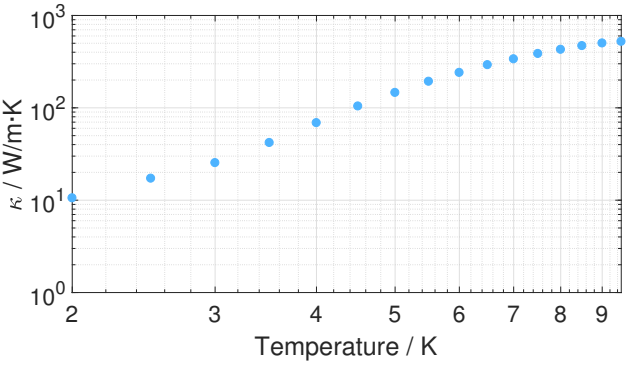

Figure 15: Thermal conductivity vs. temperature of the QPR sample tube.

some values exhibit significant deviations from the expected curves, likely due to problems during the fitting procedure of these particular spectra. The net change in penetration depth λ was deduced based on the previous results, as depicted in Fig. 14. It confirms that the net change of penetration depth stays independent of the frequency, as expected.

Thermal Conductivity

The final measurement conducted corresponded to the thermal conductivity κ of the sample as a function of temperature (see Fig. 15). κ was deduced by measuring the DC heating of the sample $\dot{Q}$, provided with the heater, and recording the temperature of sensors T_1 and T_4, as observed in Fig. 3. Note that the obtained κ value corresponds to that of the sample cylinder. The thermal conductivity is obtained from Fourier's law of heat conduction, which is expressed as

$$\dot{Q} = -\kappa\,(T)\,A\frac{\partial T}{\partial z}, \tag{6}$$

where A is the cross-sectional area of the sample cylinder and z is the coordinate indicates the path the heat travels along the sample, which the distance from T_1 and T_4. The *RRR* and the mean free path ℓ of this section of the sample were calculated with [20]:

$$RRR = 4 \cdot \kappa\,(4.2\,\mathrm{K}) = 327.93 \pm 2.86$$

and

$$\ell = 2.7 \cdot RRR = (885.40 \pm 7.73)\,\mathrm{nm}.$$

The *RRR* appears to be in good agreement to the known purity of the sample studied, which is assumed to be 300.

Material Parameters of the Sample

The previous findings allowed for the determination of the sample material parameters, which are reported in Table 3.

The obtained values of Δ_0/k_BT_c and $\lambda_L(0\,K)$ are in good accordance with literature values [29] for a Nb sample. The investigation of the frequency-dependent R_{res} is ongoing. Typically, R_{res} is reported without such dependency. However, this behaviour could indicate the possibility of trapped flux as the underlying cause [30]. This results underscore the powerful capabilities of the QPR and its great value in SRF accelerator R&D.

Table 3: Calculated Material Properties of the Sample, with $\lambda_0 = \lambda_L(0\,\mathrm{K})$, $k_B = 1.38 \times 10^{-23}$ J/K, and $T_c = 9.27$ K

f / MHz	424	857	1298
Δ_0/k_BT_c	2.05±0.19	2.02±0.27	1.95±0.35
R_{res} / nΩ	21.22±0.44	88.46±4.59	292.04±1.58
RRR	239.87±20.11	292.80±4.42	210.58±14.51
ℓ / nm	647.65±54.30	790.56±11.93	568.57±39.15
λ_0 / nm	38.12±0.01	39.50±0.05	38.77±0.01
λ_{eff} / nm	40.13±0.11	39.93±0.11	40.28±0.11

SUMMARY

Sample characterization plays a crucial role as a preliminary step prior to coating an entire cavity or implementing new heat treatments. Test devices that enable such studies significantly contribute to the advancement of Nb-alternatives in the field of accelerator R&D. To facilitate systematic studies of superconducting samples across the frequency f, temperature T, and magnetic field B, a collaborative effort between Universität Hamburg and DESY has led to the development and construction of an improved Quadrupole Resonator.

The UHH QPR, skilfully manufactured at Zanon and successfully commissioned at DESY, enables comprehensive investigations of superconducting samples. Through design optimization, this system offers simplified operation thanks to its reduced detuning and minimizes parasitic heat on the sample RF surface.

The characterization of a niobium sample led to the determination of material parameters that exhibit excellent agreement with literature values for a niobium sample with "Q-disease". Ongoing analysis includes the study of frequency-dependent residual resistance. These findings highlight the QPR's powerful capabilities and its valuable role in SRF accelerator research and development.

ACKNOWLEDGMENTS

The authors would like to thank SRF R&D teams at Universität Hamburg, DESY, HZB, CERN, TEMF, Universität Rostock, and Jefferson Lab.

This work was supported by the BMBF under the research grants 05H18GURB1, 05K19GUB, and 05H2021.

This work was also supported by the Helmholtz Association within the topic Accelerator Research and Development (ARD) of the Matter and Technologies (MT) Program.

REFERENCES

[1] A. M. Valente-Feliciano, "Superconducting RF materials other than bulk niobium: a review", *Supercond. Sci. Technol.*, vol. 29, no. 11, p. 113002, 2016. doi:10.1088/0953-2048/29/11/113002

ISBN: 978-3-95450-234-9 ISSN: 2673-5504 doi:10.18429/JACoW-SRF2023-THCAA02

[2] S. Keckert, "Characterization of Nb_3Sn and Multilayer Thin Films for SRF Applications", Ph.D. thesis, University Siegen, Siegen, Germany, 2019.

[3] A. Gurevich, "Enhancement of rf breakdown field of superconductors by multilayer coating", *Appl. Phys. Lett.*, vol. 88, p. 012511, 2006. doi:10.1063/1.2162264

[4] A. Grassellino *et al.*, "Nitrogen and argon doping of niobium for superconducting radio frequency cavities: a pathway to highly efficient accelerating structures", *Supercond. Sci. Technol.*, vol. 26, no. 10, p. 102001, 2013. doi:10.1088/0953-2048/26/10/102001

[5] A. Grassellino *et al.*, "Unprecedented quality factors at accelerating gradients up to 45 MV/m in niobium superconducting resonators via low temperature nitrogen infusion", *Supercond. Sci. Technol.y*, vol. 30, no. 9, p. 094004, 2017. doi:10.1088/1361-6668/aa7afe

[6] S. Posen, A. Romanenko, A. Grassellino, O. S. Melnychuk, and D. A. Sergatskov, "Ultralow Surface Resistance via Vacuum Heat Treatment of Superconducting Radio-Frequency Cavities", *Phys. Rev. Appl.*, vol. 13, p. 014024, 2020. doi:10.1103/PhysRevApplied.13.014024

[7] P. Goudket, T. Junginger, and B. P. Xiao, "Devices for SRF material characterization", *Supercond. Sci. Technol.*, vol. 30, no. 1, p. 013001, 2016. doi:10.1088/0953-2048/30/1/013001

[8] E. Brigant, E. Haebel, and E. Mahner, "The Quadrupole Resonator, Design Considerations and Layout of a New Instrument for the RF Characterization of Superconducting Surface Samples", in *Proc. EPAC'98*, Stockholm, Sweden, Jun. 1998, paper TUP042B, pp. 1855-1857.

[9] T. Junginger, "Investigations of the surface resistance of superconducting materials", Ph.D. thesis, Ruprecht-Karls-Universität, Heidelberg, Germany, 2012.

[10] R. Kleindienst, J. Knobloch, and O. Kugeler, "Development of an Optimized Quadrupole Resonator at HZB", in *Proc. SRF'13*, Paris, France, Sep. 2013, paper TUP074, pp. 614-616.

[11] S. Keckert, R. Kleindienst, O. Kugeler, D. Tikhonov, and J. Knobloch, "Characterizing materials for superconducting radiofrequency applications—A comprehensive overview of the quadrupole resonator design and measurement capabilities", *Rev. Sci. Instrum.*, vol. 92, p. 064710, 2021. doi:10.1063/5.0046971

[12] V. del Pozo Romano, R. Betemps, F. Gerigk, R. Illan Fiastre, and T. Mikkola, "Redesign of CERN's Quadrupole Resonator for Testing of Superconducting Samples", in *Proc. SRF'17*, Lanzhou, China, Jul. 2017, pp. 420-422. doi:10.18429/JACoW-SRF2017-TUPB016

[13] M. Arzeo, "Design, manufacturing and evaluation of the 2nd CERN quadrupole resonator", presented at Quadrupole Resonator Workshop, Berlin, Germany, 2019.

[14] P. Putek, S. G. Zadeh, M. Wenskat, and U. van Rienen, "Multi-objective design optimization of a Quadrupole Resonator under uncertainties", 2020. doi:10.48550/arXiv.2004.09470

[15] S. Bira, "Geometry Optimization for a Quadrupole Resonator at Jefferson" presented at SRF'23, Grand Rapids, MI, USA, Jul. 2023, paper WEPWB048, this conference.

[16] E. Haebel *et al.*, "Cavity shape optimization for a superconducting linear collider", in *Proc. HEACC'92*, Hamburg, Germany, Jul. 1992, p. 957.

[17] W. Singer *et al.*, "Specification Documents for Production of European XFEL 1.3 GHz SC Cavities", DESY, Germany, 2009.

[18] T. O. Raubenheimer, "The LCLS-II-HE, A High Energy Upgrade of the LCLS-II", in *Proc. FLS'18*, Shanghai, China, Mar. 2018, pp. 6–11. doi:10.18429/JACoW-FLS2018-MOP1WA02

[19] H. T. Hou *et al.*, "SRF Status of the SHINE Project at Shanghai", presented at SRF'19, Dresden, Germany, Jul. 2019.

[20] H. Padamsee, J. Knobloch, and T. Hays, *RF Superconductivity for Accelerators*, 2nd Ed. Weinheim, Germany: Wiley-VCH Verlag, 2008.

[21] M. Martinello *et al.*, "Advancement in the Understanding of the Field and Frequency Dependent Microwave Surface Resistance of Niobium", in *Proc. SRF'17*, Lanzhou, China, Jul. 2017, pp. 364-367. doi:10.18429/JACoW-SRF2017-TUYAA02

[22] R. Kleindienst, "Radio Frequency Characterization of Superconductors for Particle Accelerators", Ph.D. thesis, Universität Siegen, Siegen, Germany, 2017.

[23] S. Keckert *et al.*, "Mitigation of parasitic losses in the quadrupole resonator enabling direct measurements of low residual resistances of SRF samples", *AIP Adv.*, vol. 11, p. 125326, 2021. doi:10.1063/5.0076715

[24] S. Keckert, T. Junginger, J. Knobloch, and O. Kugeler, "The Challenge to Measure nΩ Surface Resistance on SRF Samples", in *Proc. IPAC'18*, Vancouver, Canada, Apr.-May 2018, pp. 2812-2815. doi:10.18429/JACoW-IPAC2018-WEPML049

[25] J. Knobloch, "The "Q disease" in Superconducting Niobium RF Cavities", *AIP Conf. Proc.*, vol. 671, p. 133, 2003. doi:10.1063/1.1597364

[26] M. Wiencek, K. Kasprzak, D. Kostin, D. Reschke, and L. Steder, "Summary of the Superconducting Rf Measurements in AMTF Hall at DESY", presented at SRF'23, Grand Rapids, MI, USA, Jun. 2023, paper MOPMB058, this conference.

[27] S. Bira *et al.*, "Multipacting Analysis of the Quadripolar Resonator (QPR) at HZB", in *Proc. SRF'21*, East Lansing, MI, USA, Jun.-Jul. 2021, p. 42. doi:10.18429/JACoW-SRF2021-SUPCAV013

[28] J. C. Slater, "Microwave Electronics," *Rev. Mod. Phys.*, vol. 18, p. 04441, 1946. doi:10.1103/RevModPhys.18.441

[29] B. W. Maxfield and W. L. McLean, "Superconducting Penetration Depth of Niobium", *Phys. Rev.*, vol. 139, 1965. doi:10.1103/PhysRev.139.A1515

[30] M. Checchin *et al.*, "Frequency dependence of trapped flux sensitivity in SRF cavities", *Appl. Phys. Lett.*, vol. 112, p. 072601, 2018. doi:10.1063/1.5016525